Energy Storage Materials 67 (2024) 103262

Contents lists available at ScienceDirect

Energy Storage Materials

journal homepage: www.elsevier.com/locate/ensm

Impact of degradation mechanisms at the cathode/electrolyte interface of garnet-based all-solid-state batteries

Moritz Clausnitzer [*,a,b], Martin Ihrig [c], Luca Cressa [d], Simon Hein [a,b], Martin Finsterbusch [e], Santhana Eswara [d], Liang-Yin Kuo [f], Timo Danner [a,b], Payam Kaghazchi [e], Dina Fattakhova-Rohlfing [e], Olivier Guillon [e], Arnulf Latz [a,b,g]

[a] German Aerospace Center (DLR), Institute of Engineering Thermodynamics, Stuttgart, 70569, Germany
[b] Helmholtz Institute Ulm for Electrochemical Energy Storage (HIU), Ulm, 89081, Germany
[c] Department of Chemical Engineering, National Taiwan University of Science and Technology, Taipei City, 106, Taiwan
[d] Luxembourg Institute of Science and Technology, Advanced Instrumentation for Nano-Analytics (AINA), Belvaux, 4422, Luxembourg
[e] Forschungszentrum Jülich GmbH, Institute of Energy and Climate Research, Materials Synthesis and Processing (IEK-1), Jülich, 52425, Germany
[f] Ming Chi University of Technology, Department of Chemical Engineering, New Taipei City, 24301,Taiwan
[g] Ulm University, Institute of Electrochemistry, Ulm, 89081, Germany

ARTICLE INFO

Keywords:
All-solid-state batteries
Composite cathode
Continuum modeling
Interface degradation
Cathode/garnet interface

ABSTRACT

All-solid-state batteries have the potential to improve the safety, energy-, and power density of lithium-ion batteries. However, the limited stability of rigid solid-solid interfaces remains a key challenge. The cathode/electrolyte interface is particularly prone to degradation during high-temperature sintering and electrochemical cycling, forming secondary phases that impede charge transport and limit cell performance. Experimental analysis of these phases is challenging since they result in thin resistive films that are sensitive to typical characterization techniques. In this study, we use structure-resolved electrochemical simulations to investigate the impact of resistive phases at the cathode/electrolyte interface on cell performance and identify dominant degradation mechanisms. We extend our simulation framework with a novel resistive film model that accounts for the additional charge transfer resistance at the interface based on interphase properties. Our approach combines continuum simulations with insights from density functional theory and experimental data, including secondary ion mass spectrometry measurements. This allows us, for the first time, to assess the impact of resistive films on the degradation of full-cell performance.

1. Introduction

All-solid-state batteries (ASSBs) are a promising technology for next-generation energy storage systems [1–4]. Compared to conventional lithium-ion batteries (LIBs) with liquid electrolytes, ASSBs offer the potential to improve operational safety by employing solid electrolytes and increase energy density by enabling the use of lithium metal anodes. However, ASSBs have yet to reach their full potential due to several limitations that undermine cell performance. A major concern is degradation at the various rigid solid/solid interfaces, which can lead to increased interfacial resistance and reduced practical capacity [5–8].

Due to the large contact area between the solid electrolyte (SE) and cathode active material (CAM) in the composite cathode, the cathode-electrolyte interface is a key interface for cell operation. However, during manufacturing and cell operation, the cathode-electrolyte interface is susceptible to parasitic chemical reactions, electrochemical oxidation, and chemo-mechanical degradation [9]. These degradation processes significantly degrade interfacial properties and can lead to rapid capacity fading during cycling.

A promising SE is the garnet $Li_7La_3Zr_2O_{12}$ (LLZO), noted for its high electrochemical stability window [8,10], good stability against Li metal [9] and highly conductive cubic phase that can be stabilized at room temperature with dopants such as aluminum and tantalum [11–15]. The manufacturing of garnet-based composite cathodes typically involves high-temperature co-sintering to ensure intimate contact between individual SE and CAM particles. Such elevated temperatures can cause stability issues at the SE/CAM interface, where chemical reaction kinetics and elemental interdiffusion are accelerated, potentially resulting

* Corresponding author.
E-mail address: moritz.clausnitzer@dlr.de (M. Clausnitzer).

https://doi.org/10.1016/j.ensm.2024.103262
Received 22 December 2023; Received in revised form 26 January 2024; Accepted 13 February 2024
Available online 21 February 2024

in the formation of a cathode/electrolyte interphase [9]. Among various cathode active materials (CAMs), $LiCoO_2$ (LCO) has demonstrated enhanced interfacial stability with LLZO [16–19]. However, recent studies have shown interdiffusion across the LCO/LLZO interface at temperatures below typical sintering temperatures of LCO/LLZO composites [9]. Experimental and computational studies suggest degradation products such as La_2O_3, $La_2Zr_2O_7$, and $LaCoO_3$, which are likely to have poor Li-ion conductivity [9,18–21]. Consequently, these secondary phases increase charge transfer resistance and reduce cell performance [21,22]. It is important to note that the reported onset temperature for degradation, the specific reaction products, and the extent of forming layers vary significantly between different experimental studies [19,21,23].

Several strategies have been proposed to mitigate thermally induced degradation. These include the use of sinter-aids and dopants [16,24–26], low-temperature infiltration of CAM into an LLZO scaffold [27], and rapid thermal processing [28,29].

Furthermore, the LCO/LLZO interface is susceptible to electrochemical degradation during cycling. Cation diffusion across the interface can lead to the growth of a resistive phase at the SE/CAM interface and loss of LLZO crystallinity [30,31]. Theoretical calculations suggest that the LLZO/LCO interface may not be electrochemically stable during electrochemical cycling, depending on dopants and sintering additives [18,20,30]. Moreover, volume changes in the CAM during cycling generate compressive and tensile stresses in the composite cathode, potentially causing interface delamination [32,33]. Possible crack formation and isolation of CAM particles result in a permanent loss of capacity [7,34]. In addition, microcracks have been observed in LCO grains impeding Li-ion and electron transport. These defects might originate from oxygen vacancies in the LCO created during high-temperature sintering [32].

Both degradation during processing and operation can lead to the formation of a resistive cathode/electrolyte interphase, resulting in diminished cell performance. Yet, understanding and distinguishing the various degradation mechanisms and assessing their impact on performance loss is very challenging. Experimental analysis is impeded by the nanoscale thickness of resistive layers and the sensitivity of LLZO to characterization techniques using fast electrons. Due to these constraints, simulations are an important tool for identifying underlying mechanisms.

In conventional Li-ion batteries, continuum modeling has proven effective for studying solid electrolyte interphase (SEI) formation [35,36]. Drawing from these concepts, our study introduces a new simulation approach to investigate the influence of degradation products in ASSBs using structure-resolved continuum simulations. Specifically, we introduce an efficient resistive film model capturing the effect of resistive interfaces in microstructure-resolved simulations.

Fig. 1 illustrates the workflow and methods employed in this study. Our research primarily focuses on two distinct phenomena: 1) the degradation occurring during the processing of high-temperature processed LCO/LLZO electrodes and 2) the electrochemical degradation during the operation of low-temperature processed LCO/LLZO electrodes. For each case, we generate a FIB-SEM reconstruction of an exemplary LCO/LLZO composite cathode, which serves as the input for our 3D simulations. The first sample, fabricated through high-temperature sintering, is studied to understand performance loss mainly attributable to thermal degradation during manufacturing [22]. The second sample is manufactured by field-assisted sintering/spark plasma sintering (FAST/SPS) at reduced sintering temperature to avoid thermal degradation and is used to investigate performance loss due to electrochemical degradation during cell operation. Our simulation model is parameterized based on experimental results from Refs. [22,29]. Additionally, our simulations are informed by Secondary Ion Mass Spectrometry (SIMS) measurements and Density Functional Theory (DFT) calculations. This synergistic approach improves model predictions and aids in the interpretation of performance-limiting processes in both uncycled and cycled composite cathodes.

Overall, this study emphasizes the importance of understanding different degradation mechanisms in composite cathodes of garnet-based ASSBs. This facilitates the evaluation, comparison, and enhancement of cathode fabrication and design. Although we focus on the material system LCO/LLZO, the methods and results presented in this study apply to other rigid SEs and CAMs as well.

2. Experimental section

Cell manufacturing and characterization Two types of composite cathodes were investigated in this study. The first cathode, labeled as HT in the following, is composed of LCO-LLZO:Ta ($Li_{6.6}La_3Zr_{1.6}Ta_{0.4}O_{12}$) and was produced via high-temperature sintering. Upon manufacturing, the cathode was assembled with an LLZO:Ta separator and a Li metal foil. Details are given in Ref. [22]. The second cathode, referred to as sample LT, was fabricated using FAST/SPS, employing a lower sintering temperature. Notably, the LLZO in this cathode was doped with Aluminum, resulting in an LLZO:Al,Ta ($Li_{6.45}Al_{0.05}La_3Zr_{1.6}Ta_{0.4}O_{12}$) composition. This cathode was assembled with an LLZO:Al,Ta separator and an In anode. Further details are provided in Refs. [29,30]. Comprehensive results of physical, chemical, and electrochemical characterization of the cells are published in Refs. [22,29–31].

Secondary ion mass spectrometry LCO-LLZO:Al,Ta composite cathode

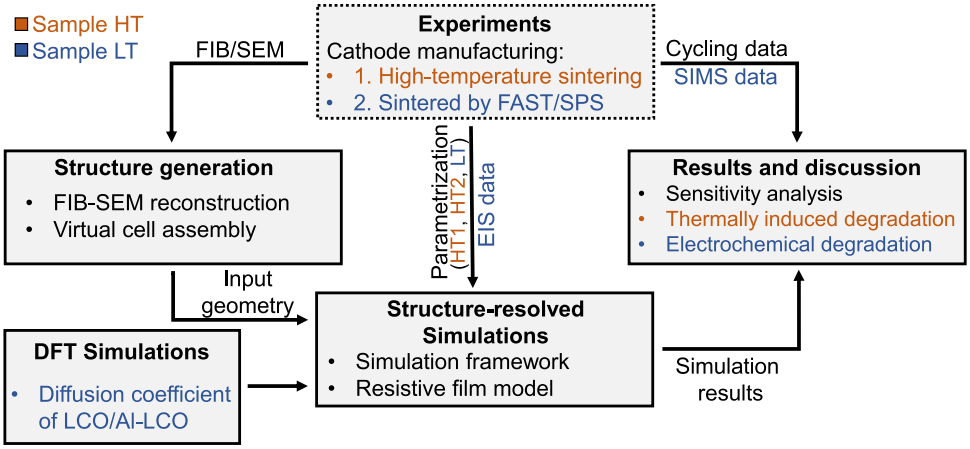

Fig. 1. Schematic overview of the workflow in this study. Measured discharge curves for the composite cathode sintered using conventional methods are adapted from Ref. [22]. EIS data and electrochemical discharge curves for the composite cathode sintered by FAST/SPS are adapted from Ref. [30]. Different parameter sets (HT1, HT2, LT) are used in our simulations to reproduce and interpret the experimental data.

samples, sintered via FAST/SPS, were analyzed using SIMS before and after cycling (10 cycles). The measurements allow us to gain insights into the elemental redistribution of Co, La, and Al subsequent to fabrication and cycling. Detailed information on the experimental procedure is available in Ref. [31].

3. Simulation section

We study the effect of secondary phases in the composite cathode by employing structure-resolved simulations. Using the Battery and Electrochemistry Simulation Tool (BEST), we are able to correlate microstructure, material parameters, and electrochemical cell performance [37].

3.1. Structure generation

The composite cathode effectively determines the energy and power density of the battery cell, requiring careful optimization of its microstructure [38–44]. Our simulations use reconstructions of the cathode microstructure as simulation domain. Therefore, we directly include structural properties such as volume fractions, particle sizes, and pores.

3D reconstructions for both cathode samples, HT and LT, were obtained using FIB-SEM tomography. The resulting image stacks were processed using image registration, cropping, and filtering. The images were then segmented into CAM, SE, and pores based on grayscale values. The grayscale thresholds were adjusted in line with the experimentally determined cathode composition and visual evaluations to ensure an accurate reconstruction.

Fig. 2 displays the final 3D reconstructions of the two composite cathodes. A detailed overview of the structural properties of both electrodes can be found in Table 1. The reconstruction of sample HT has a higher CAM fraction than sample LT. Both structures display high density after sintering, with sample LT achieving an exceptional density of 96%. It is important to note that FIB-SEM imaging of Sample LT revealed noticeable cracks in both the LCO and LLZO phases. However, both visual examination and detailed imaging conducted in a previous study revealed no evidence of cracking in the samples [30]. Therefore, we attribute these discrepancies to the handling of the samples prior to the FIB-SEM measurements. Minor cracks were rectified using a medium filter to ensure a representative geometry for our simulations. The remaining cracks in the reconstructions do not significantly affect the fraction of isolated CAM particles that are not connected to the cathode current collector. For both reconstructions HT and LT, the fraction of inactive, disconnected CAM particles is less than 1%.

Figure S1 illustrates the workflow to obtain our simulation input structure from the FIB-SEM images. Since FIB-SEM measurements only capture a limited segment of the cathode, we mirrored the obtained 3D reconstructions to match the thickness observed in SEM cross-sections. To complete the input structures, we added an isotropic electrolyte separator pellet, a Li metal anode, and current collectors.

Table 1
Characteristics of the 3D reconstructions for sample HT and LT. The reconstructed microstructures were mirrored to achieve the experimental electrode length.

Symbol	Short description	Unit	Sample HT	Sample LT
l_x	Cathode length in x-direction	μm	11	26
l_y	Cathode length in y-direction	μm	25	35
l_z	Cathode length in z-direction	μm	16	28
ϵ_{CAM}	CAM volume fraction	%	63	53
ϵ_{SE}	SE volume fraction	%	30	43
ϵ_0	Pore volume fraction	%	7	4
$l_{x,exp}$	Experimental electrode length	μm	25	35

3.2. Electrochemical simulations

Based on the generated 3D reconstructions, we conduct structure-resolved simulations to study the effect of degradation phases. The mass and charge transport in the battery cell is calculated using the in-house code BEST. The code uses a set of partial differential equations derived from the respective conservation laws to calculate mass and charge transport in the active material (AM) and SE phase [45,46]. The set of constitutive equations is summarized in Table 2.

3.2.1. Standard interface model

To describe the charge transport at the CAM/SE interface in our standard simulation case, we use a Butler-Volmer-expression. Eq. (1) relates the interfacial current i_{BV} to the exchange current density i_0 and surface overpotential η.

$$i_{BV} = i_0\left[\exp\left(\frac{\alpha F}{RT}\eta\right) - \exp\left(-\frac{(1-\alpha)F}{RT}\eta\right)\right] \quad (1)$$

Table 2
Governing equations used in BEST [37,45].

Equation	Short description
Transport in active material	
$\frac{\partial c_{AM}}{\partial t} = -\nabla\cdot(-D_{Li}^{AM}\nabla c_{Li}^{AM})$	Mass balance
$0 = -\nabla\cdot i^{AM}$	Charge balance
$i_{AM} = -\sigma_{Li}^{AM}\nabla\Phi^{AM}$	Electric current
Transport in solid electrolyte ($t_{Li}^{+} = 1$)	
$0 = -\nabla\cdot i^{SE}$	Charge balance
$i_{SE} = -\kappa_{Li}^{SE}\nabla\varphi^{SE}$	Ionic current
Interface between AM and SE	
$i_{BV} = i_0\left[\exp\left(\frac{\alpha F}{RT}\eta\right) - \exp\left(-\frac{(1-\alpha)F}{RT}\eta\right)\right]$	Butler-Volmer current
$i_0 = i_{00}^{AM} c_{SE}^{\alpha} c_{AM}^{\alpha} (c_{AM}^{max} - c_{AM})^{1-\alpha}$	Exchange current density

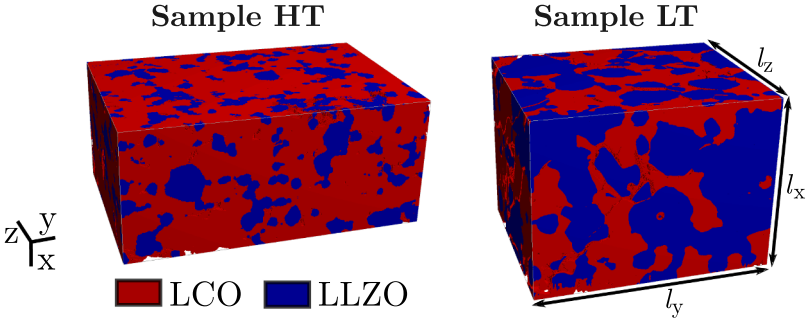

Fig. 2. 3D FIB-SEM reconstructions of two composite cathodes. Sample HT was manufactured at high temperatures and long dwell times [22]. Sample LT was sintered with FAST-SPS at elevated pressures and reduced sintering temperatures and dwell time [29]. Structural properties of the reconstructions are summarized in Table 1.

The exchange current density i_0 depends on the Li-ion concentration of SE and CAM and can be calculated according to Eq. (2). i_{00}^{CAM} is the exchange current density factor, α denotes the symmetry factor of the reaction. c_{SE} and c_{CAM} refer to the local Li-ion concentration in the SE and CAM, respectively.

$$i_0 = i_{00}^{\mathrm{CAM}} c_{\mathrm{SE}}^{\alpha} c_{\mathrm{CAM}}^{\alpha} \left(c_{\mathrm{CAM}}^{\max} - c_{\mathrm{CAM}}\right)^{1-\alpha} \tag{2}$$

The local surface overpotential is calculated from the difference of the CAM and SE potential Φ_{CAM}, φ_{SE} and open-circuit voltage U_0 and, thus, gives the deviation from the electrochemical equilibrium at the interface (Eq. (3)). Note that U_0 depends on the Li-ion concentration of the CAM and changes during the simulation.

$$\eta = \Phi_{\mathrm{CAM}} - \varphi_{\mathrm{SE}} - U_0(c_{\mathrm{CAM}}) \tag{3}$$

3.2.2. Resistive film model

Using experimental techniques, analyzing thin interlayers resulting from elemental interdiffusion across the SE/CAM interface is very challenging. To better comprehend the impact of degradation mechanisms on cell performance, we incorporate a parametric resistive film model in our simulation framework. To determine the influence of secondary phases at the electrode level, our model addresses the resolution limitations of thin layers (≈100 nm) and the high computational cost of spatially resolving the electrode microstructure. This new model implicitly solves the introduced kinetic limitations by altering the standard description of charge transfer kinetics at the SE/CAM interface.

The model considers the presence of a thin resistive film of secondary phases at the SE/CAM interface that impedes charge transfer. Depending on the electrochemical properties of the degradation products, these secondary phases will have different effects on mass and charge transport [6,47]. Fig. 3 shows a schematic of the resistive film model and highlights different scenarios that can be described by our simulation approach. The ideal interface is shown in the first schematic of Fig. 3 (a). The second case represents a degraded SE interface layer with poor ionic conductivity. The third case describes a degraded CAM interface layer with poor electronic conductivity and Li-ion mobility. Finally, the last scenario combines both interface models, providing a generalized description of resistive interface layers.

Note that the properties of the interphase itself affect the growth mechanism upon further cycling. Ideally, an interlayer forms with high ionic and low electric conductivity that stabilizes after reaching a certain thickness, hence effectively extending the electrochemical stability window of the SE [6]. As shown in Fig. 3 (b), our model describes the resistive film with five parameters: thickness, electrical conductivity, and diffusivity of a degraded CAM phase, as well as thickness and ionic conductivity of a degraded SE phase.

Degraded CAM phase According to Eqs. (1)–(3), the current at the SE/CAM interface depends on the exchange current density and open circuit voltage of the CAM, which are both a function of the surface Li-ion concentration $c_{\mathrm{Li}}^{\mathrm{CAM}}$. However, the presence of a degraded CAM phase will cause a concentration gradient over the resistive film, depending on its thickness $l_{\mathrm{RF}}^{\mathrm{CAM}}$ and effective diffusivity $D_{\mathrm{RF}}^{\mathrm{CAM}}$. The surface concentration at the resistive film $c_{\mathrm{Li}}^{\mathrm{RF}}$ can be calculated according to Eq. (4) by assuming that the intercalation flux $N_{\mathrm{BV,RF}}$ (Eq. (5)) is equal to the diffusive flux.

$$c_{\mathrm{Li}}^{\mathrm{RF}} = c_{\mathrm{Li}}^{\mathrm{CAM}} - \frac{N_{\mathrm{BV,RF}}}{D_{\mathrm{RF}}^{\mathrm{CAM}}} l_{\mathrm{RF}}^{\mathrm{CAM}} \tag{4}$$

$$N_{\mathrm{BV,RF}} = \frac{i_{\mathrm{BV,RF}}}{F} \tag{5}$$

Furthermore, the degraded CAM film hinders electron transport due to its low electrical conductivity $\sigma_{\mathrm{RF}}^{\mathrm{CAM}}$. The additional resistance can be calculated according to Eq. (6) from the film thickness and conductivity:

$$R_{\mathrm{elec}} = \frac{l_{\mathrm{RF}}^{\mathrm{CAM}}}{\sigma_{\mathrm{RF}}^{\mathrm{CAM}}} \tag{6}$$

Degraded SE phase Similarly, in the case of a SE phase, ionic transport is impeded by a film with additional ionic resistance with the thickness $l_{\mathrm{RF}}^{\mathrm{SE}}$ and ionic conductivity $\kappa_{\mathrm{RF}}^{\mathrm{SE}}$ (Eq. (7)).

$$R_{\mathrm{ion}} = \frac{l_{\mathrm{RF}}^{\mathrm{SE}}}{\kappa_{\mathrm{RF}}^{\mathrm{SE}}} \tag{7}$$

Extended BV kinetics The additional resistivities are included as the current-dependent resistance R_{RF} in the overpotential. They can be regarded as contributions of the interfacial film that limit the charge

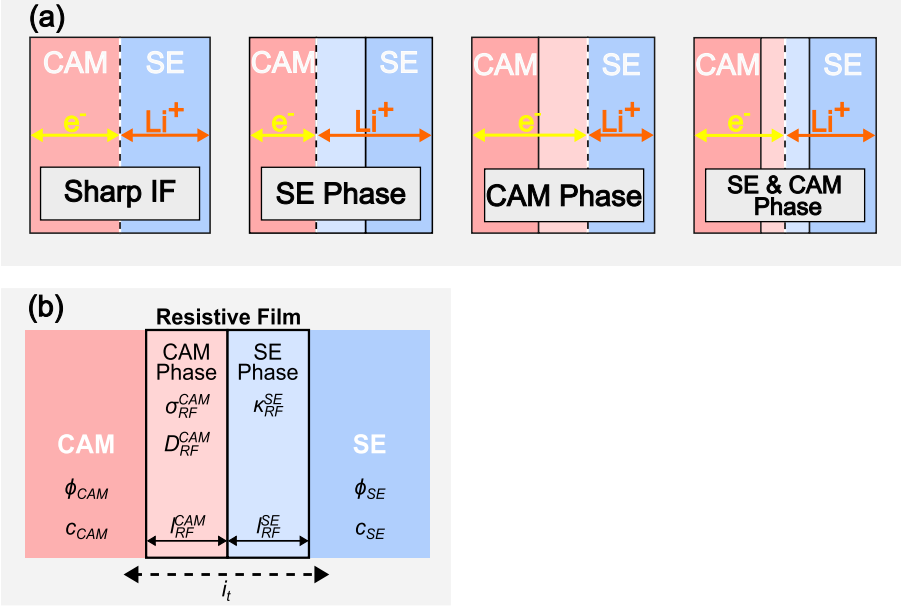

Fig. 3. (a) Overview of the different simulation cases: A sharp interface corresponding to the standard simulation case, a degraded SE phase with high ionic and low electric conductivity, a degraded CAM phase with low ionic and high electric conductivity and a combined case with both a degraded SE and CAM phase. (b) Overview of the implemented resistive film model. The resistive film is described with two parameters for a degraded SE phase and three parameters for a degraded CAM phase.

transfer kinetics at the interface (Eqs. (8)–(10)).

$$i_{\mathrm{BV,RF}} = i_0 \left[\exp\left(\frac{\alpha F}{RT}\eta_{\mathrm{RF}}\right) - \exp\left(-\frac{(1-\alpha)F}{RT}\eta_{\mathrm{RF}}\right)\right] \tag{8}$$

$$\eta_{\mathrm{RF}} = \Phi_{\mathrm{AM}} - \varphi_{\mathrm{SE}} - U_0\left(c_{\mathrm{Li}}^{\mathrm{RF}}\right) - i_{\mathrm{BV,RF}} R_{\mathrm{RF}} \tag{9}$$

$$R_{\mathrm{RF}} = R_{\mathrm{elec}} + R_{\mathrm{ion}} \tag{10}$$

3.3. Parametrization

In this study, we focus on the material system LCO/LLZO and carefully parametrize our model for these materials. In Section 4, we compare our simulation results to discharge curves from Finsterbusch et al. (at 100 and 25 °C) [22] and Ihrig et al. (at 80 °C) [30]. Therefore, we use three different parameter sets to parametrize our model for the corresponding simulation cases:

- Parameter set HT1: Composite cathode sintered conventionally and discharge at 100 °C as per Ref. [22]
- Parameter set HT2: Composite cathode sintered conventionally and discharge at 25 °C as per Ref. [22]
- Parameter set LT: Composite cathode sintered with FAST/SPS and discharge at 80 °C as per Ref. [30]

Parameters for HT1 and HT2 are taken from Ref.[22]. We build upon the study presented therein by integrating our resistive film model, which allows for a more comprehensive analysis of degradation phenomena not previously captured.

To parameterize our simulations for the low-temperature sintering case LT, we rely on electrochemical impedance data measured at 80 °C [30]. From fitting the electrochemical impedance spectroscopy (EIS) data for a plain LCO cathode on a SE pellet, the areal resistances of bulk, grain boundary, LCO/LLZO interface, and LLZO/In-Li interface were determined, representing parameter set LT. Further information on this approach can be found in the SI.

Table 3 summarizes the parameter sets HT1, HT2, and LT, along with their references. Any deviations from these parameters are noted in the relevant section.

Table 3
Parameters used for the electrochemical simulations. We use three different parameter sets: HT1: Sintered conventionally and operation at 100 °C. HT2: Sintered conventionally and operation at 25 °C. LT: Sintered by FAST/SPS and operation at 80 °C. Functional parameters are indicated by * and are given at initial conditions.

Symbol	Value	Ref.	Unit	Short description
Li metal				
U_0^{An}	0	-	V	Open circuit potential
$\sigma_{\mathrm{Li}}^{\mathrm{An}}$	100	Ref. [22]	S/cm	Electronic conductivity
i_0^{Li}	HT: $1{\cdot}10^{-3}$	Ref. [22]	A/cm^2	Exchange current density
	LT: $1.2{\cdot}10^{-3}$	Calc. [30]		
α^{Li}	0.5	-	-	Symmetry factor
LLZO				
$c_{\mathrm{Li}}^{\mathrm{SE}}$	0.0384	Ref. [22]	mol/cm^3	Concentration of Li-ions
$\kappa_{\mathrm{Li}}^{\mathrm{SE}}$	HT1: $1.1{\cdot}10^{-2}$	Ref. [22]	S/cm	Li-ion bulk conductivity
	HT2: $5.4{\cdot}10^{-4}$	Ref. [22]		
	LT: $5.195{\cdot}10^{-4}$	Ref. [30]		
t_{Li}^{+}	1	-	-	Transference number
l_{sep}	HT: 500	Ref. [22]	μm	Separator thickness
	LT: 400	Ref. [30]		
LCO				
U_0^{CAM}	4.2*	Ref. [48]	V	Open circuit potential
$c_{\mathrm{Li}}^{\mathrm{CAM,0}}$	0.027058	Ref. [22]	mol/cm^3	Initial concentration of Li-ions
$c_{\mathrm{Li}}^{\mathrm{CAM,max}}$	0.051555	Ref. [49]	mol/cm^3	Maximum concentration of Li-ions
$\sigma_{\mathrm{Li}}^{\mathrm{CAM}}$	4.47*	Ref. [50]	S/cm	Electronic conductivity
$D_{\mathrm{Li}}^{\mathrm{CAM}}$	$8.48{\cdot}10^{-12}$*	Ref. [51]	cm^2/s	Li-ion diffusion coefficient
i_{00}^{CAM}	HT: 0.0981	Ref. [22]	$\frac{\mathrm{Acm}^{2.5}}{\mathrm{mol}^{1.5}}$	Exchange current density factor
	LT: 0.1599	Calc. [30]		
α^{Li}	0.5	-	-	Symmetry factor
Operating conditions				
i_{app}	HT: 0.1	Ref. [22]	mA/cm^2	Applied current density
	LT: 0.05	Ref. [30]		
U_{cut}	3.4	-	V	Cut-off voltage

4. Results and discussion

In this section, we analyze the influence of degradation products at the CAM/SE interface on electrochemical cell performance. First, we conduct a sensitivity analysis of the implemented resistive film model to identify the main processes influencing cell performance. Then, we study the performance loss upon manufacturing and cycling by comparing our simulation results with experimental data, aiming to identify the underlying degradation mechanisms. For the simulation study focusing on thermally induced degradation during cell manufacturing, we use FIB-SEM reconstruction HT and parameter sets HT1 and HT2. For studying electrochemical degradation during cell cycling, we conduct simulations on the microstructure LT using the corresponding parameter set (cf. Sections 3.1 and 3.3). For comparable simulation results, we normalize practical capacities to the theoretical capacities of the cathode samples (Equation S3).

4.1. Effect of resistive interlayers

The LLZO/LCO interface remains poorly understood, with stability issues hindering the analysis of ideal interfaces [52]. Degradation processes are strongly influenced by processing conditions and materials, affecting the extent of chemical and mechanical degradation, as well as the electrochemical properties of forming secondary phases. Therefore, parameters of resistive films forming at the CAM/SE interface still involve significant uncertainties. The thickness of the reaction zone resulting from thermally induced degradation is reported to be around 100 nm [21]. The observed reduction in cell performance is likely to be caused by changes in the electrochemical properties of both the CAM and SE at the interface [31].

4.1.1. Sensitivity analysis

To better understand the impact of electrochemical properties of resistive films on cell performance, we first perform a sensitivity analysis of our resistive film model focusing on the scenarios schematically shown in Fig. 3 (a). As previously discussed, the model incorporates two additional effects that hinder charge transfer: 1) an ohmic contribution due to increased ionic and electronic resistance at the CAM/SE interface and 2) decreased Li-ion mobility.

Ohmic contributions According to Eqs (6)–(10), the additional ohmic film resistance depends on the thickness of the interface layer and its ionic and electronic conductivity. In our simulation framework, this resistance R_{RF} is incorporated as a current dependent term in the local overpotential.

Fig. 4 illustrates the influence of an additional film resistance due to a resistive phase on the local overpotential and electrode performance. A resistive phase at the CAM/SE interface will result in a higher interfacial resistance and higher overpotentials necessary to sustain a specific reaction rate.

Fig. 4 (a) shows the additional surface overpotential required for different film resistances compared to the standard Butler-Volmer expression. Since the resistance term is current-dependent, larger deviations from the standard Butler-Volmer expression occur at higher local currents. Above a limiting current, the film resistance leads to a steep increase in surface overpotential compared to the standard simulation case. This can be interpreted as an increasing interface deactivation, which depends on the film resistance. The effect on the Faraday current $i_{\mathrm{BV,RF}}$ is minor for the smallest assumed resistance (1 $\Omega\mathrm{cm}^2$). However, the critical current density decreases significantly with increasing film resistance, becoming relevant to practical currents across the CAM/SE interface.

Fig. 4 (b) shows the discharge of a 3D cell (Sample HT) at a current density of 0.1 $\mathrm{mA/cm}^2$ with increasing film resistance. The influence of film resistance on the discharge curve is minor up to 10 $\mathrm{k\Omega\ cm}^2$. For higher film resistance, the capacity drops significantly. Fig. 4 (d) shows the current distribution in the SE phase of the composite cathode at the beginning of the simulation. At lower film resistance (R_{RF} = 100 $\Omega\ \mathrm{cm}^2$), Li-ions primarily intercalate near the separator to minimize ionic pathways and resistance. In contrast, high interfacial resistance (R_{RF} = 100 $\mathrm{k\Omega\ cm}^2$) results in an extended reaction zone with distinct local ionic current hot spots. Therefore, ionic pathways are significantly longer in the latter case, resulting in higher overpotential and lower cell performance. This implies a significant contribution of ohmic losses in the electrolyte to the higher cell polarization, although we formally increase the resistance of the interface.

In Fig. 4 (c), the effect of an additional ohmic film resistance on cell performance is shown for applied current densities ranging from 0.1 to 2 $\mathrm{mA/cm}^2$. An increasing current density leads to higher local currents at the cathode/electrolyte interface, resulting in a stronger effect of the ohmic film resistance on the cell capacity. At i_{app} = 0.1 $\mathrm{mA/cm}^2$, the cell capacity is nearly constant until $R_{\mathrm{RF}} = 1{\cdot}10^4\ \Omega\mathrm{cm}^2$. However, at i_{app} = 2 $\mathrm{mA/cm}^2$, currents at the interface are significantly higher, causing a decrease in cell capacity already at R_{RF} = 1 $\mathrm{k\Omega\ cm}^2$. Note that deactivation of surfaces, e.g., due to delamination, alleviates this problem, resulting in high local current densities. Figure S2 shows the effect of reduced interface area on discharge capacity.

Reduction of Li-ion mobility A resistive film forming due to degradation of the CAM potentially reduces the mobility and diffusion of Li-ions.

Fig. 5 (a) shows the Li-ion concentration across a film with a thickness of 100 nm according to Eq. (4). The interface between the CAM interphase and the bulk SE is located at 0 nm. The CAM particle is lithiated with a flux corresponding to 0.01 $\mathrm{mA/cm}^2$. As a result, the Li-ion concentration at the interface (0 nm) is higher than the bulk CAM concentration (100 nm). The increase in Li-ion concentration depends on both the diffusion coefficient $D_{\mathrm{RF}}^{\mathrm{CAM}}$ of the resistive film and the local current i_{BV}. At $D_{\mathrm{RF}}^{\mathrm{CAM}} = 1{\cdot}10^{-12}$ cm^2/s, $c_{\mathrm{Li}}^{\mathrm{RF}}$ is only slightly higher than $c_{\mathrm{Li}}^{\mathrm{CAM}}$. However, reducing the diffusion coefficient by an order of magnitude already leads to a significant increase in Li-ion concentration. In our resistive film model, a higher Li-ion concentration at the interface results in a lower open-circuit voltage and exchange current density, leading to reduced cell performance.

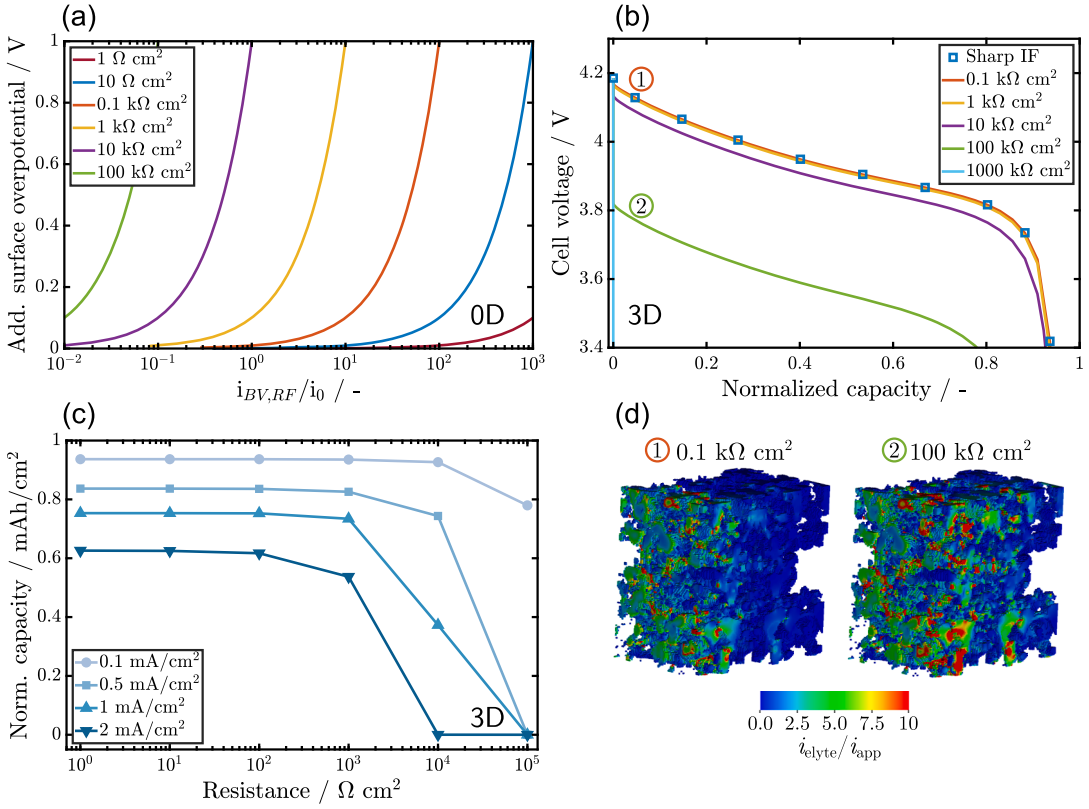

Fig. 4. Sensitivity analysis of the resistive film model considering additional ohmic contributions at the CAM/SE interface. (a) Required additional surface overpotential to achieve specific interface currents in the 0D simulation case, considering different film resistances. (b) Influence of additional film resistance on discharge curve in a 3D simulation case using the reconstructed electrode HT at a current of 0.1 $\mathrm{mA/cm}^2$. (c) Impact of film resistance on normalized capacity at applied current densities of 0.1, 0.5, 1, and 2 $\mathrm{mA/cm}^2$ in a 3D simulation based on the reconstructed sample HT. (d) Current distribution in the SE phase of the composite cathode at $t = 1s$ for $R_{\mathrm{RF}} = 0.1\ \mathrm{k\Omega\,cm}^2$ and R_{RF} = 100 $\mathrm{k\Omega\,cm}^2$, respectively. The separator is on the left, and the current collector is on the right of the depicted structures.

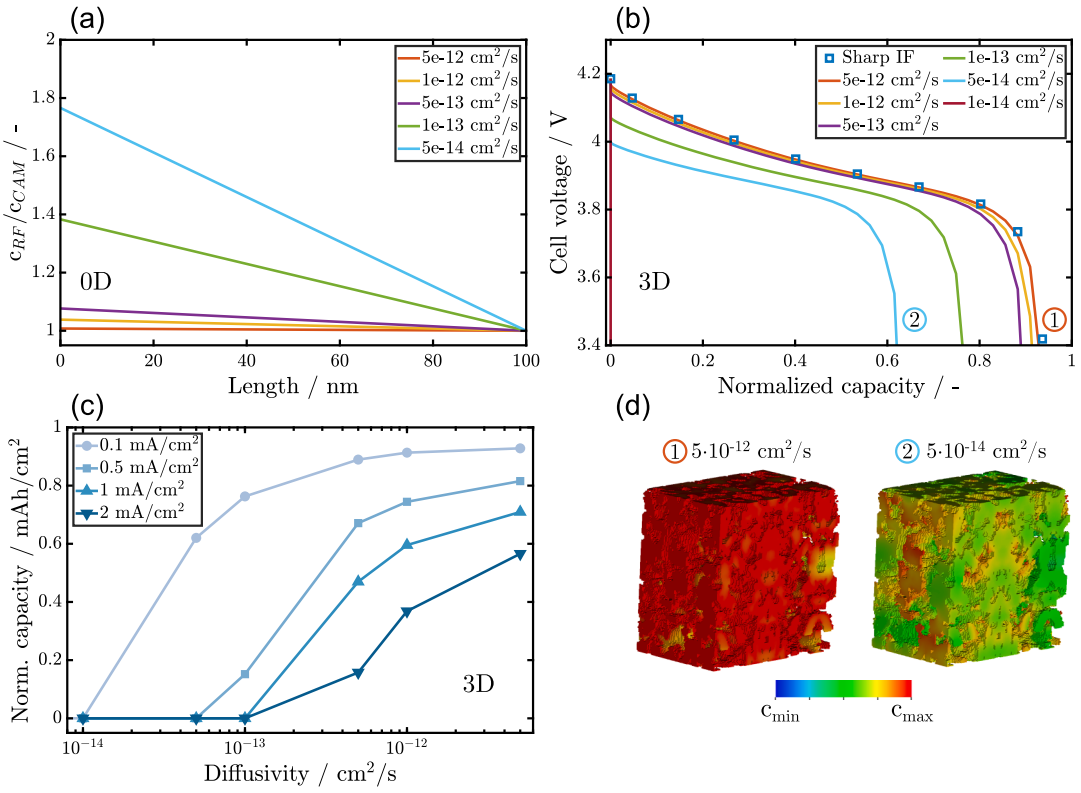

Fig. 5. Sensitivity analysis of the resistive film model with reduced Li-ion mobility at the CAM/SE interface. (a) Effect of film diffusivity on the concentration gradient across a 100-nm-thick film, considering an interface current of $i_{BV} = 0.01$ mA/cm^2 during discharge. (b) Impact of reduced Li-ion mobility on the discharge curve in a 3D simulation using the reconstructed electrode HT at a current of 0.1 mA/cm^2. (c) Normalized capacity versus Li-ion diffusivity of the resistive film for current densities between 0.1 and 2 mA/cm^2 in a 3D simulation based on the reconstruction of sample HT. (d) Li-ion concentration in the CAM phase after discharge for $D_{RF}^{CAM} = 5{\cdot}10^{-12}$ cm^2/s and $D_{RF}^{CAM} = 5{\cdot}10^{-14}$ cm^2/s, respectively. The separator is on the left, and the current collector is on the right of the depicted structures.

Fig. 5 (b) illustrates the effect of Li-ion mobility in a resistive CAM phase on the discharge curve. As the mobility of Li-ions in the resistive film decreases, the discharge curve shifts toward lower voltages and reduced capacities. Fig. 5 (d) also depicts the Li-ion concentration within the CAM at the end of discharge, comparing cases with high and low film diffusivity. Lower Li-ion mobility in the resistive film leads to elevated local overpotentials and decreased potential. Consequently, the cut-off voltage is reached at lower lithiation states of the CAM, reducing capacity significantly.

Fig. 5 (c) demonstrates the decline in normalized capacity as a result of reduced interphase mobility in the 3D simulation case for current densities ranging from 0.1 to 2 mA/cm^2. Even at low current densities, a decrease in D_{RF}^{CAM} results in a significant loss of capacity. At $i_{app} = 0.1$ mA/cm^2, the capacity drops to nearly 0 for a diffusion coefficient of $1{\cdot}10^{-14}$ cm^2/s. This effect becomes even more pronounced at higher current densities. For bulk LCO, the effective diffusion coefficient is typically between $1{\cdot}10^{-11}$ and $1{\cdot}10^{-12}$ cm^2/s depending on the lithiation state [51]. Therefore, even a thin resistive layer with slightly lower diffusivity than LCO can cause substantial capacity loss.

Minimum requirements of resistive films

Our resistive film model provides valuable insights into the minimum requirements of resistive films necessary for successful cell operation. These criteria are pertinent for both degradation and coating layers located at the SE/CAM interface. Our sensitivity analysis indicates that, at practical current densities, the tolerable ohmic resistance of the interphase is approximately $R_{RF} = 1$ kΩ cm^2. For a CAM phase, the Li-ion diffusion coefficient should not be significantly below $1{\cdot}10^{-12}$ cm^2/s at a film thickness of 100 nm.

4.2. Analysis of performance of high-temperature processed electrodes

Conventional sintering of LCO/LLZO composite cathodes usually involves high temperatures above 1000 °C to achieve densification and intimate contact between individual particles [22]. However, high temperatures accelerate secondary phase formation due to cation interdiffusion, structural changes, and chemical reactions [21]. As a result, resistive interphases are observed at the cathode/electrolyte interface, negatively impacting charge transfer and overall cell performance.

In the study by Finsterbusch et al., a high-temperature sintering step was used in the processing of LCO/LLZO composite cathodes. Utilization of the CAM was up to 81% at 100 °C and a current of 0.1 mA/cm^2 [22]. However, capacity dropped significantly at room temperature. While structure-resolved simulations showed good agreement at high operational temperatures, they could not explain the substantial performance loss at room temperature. The authors suggested that an additional charge transfer resistance at the CAM/SE interface with high activation energy is causing the capacity loss [22]. Building on this hypothesis, our study introduces a refined simulation model that incorporates a detailed characterization of the interfacial resistance.

To gain a better understanding of the relevant processes and transport limitations, we performed electrochemical simulations on the FIB-SEM reconstruction of sample HT (cf. Section 3.1) using the resistive film model. Our main working hypothesis is that a homogeneous resistive layer forms at the CAM/SE interface due to the high-temperature sintering step, blocking charge transfer at low operating temperatures.

Fig. 6 (a) presents a comparison between our simulation results for a discharge current of 0.1 mA/cm^2 and the experimental data from Finsterbusch et al. [22] at temperatures of 100 °C and 25 °C. Using the

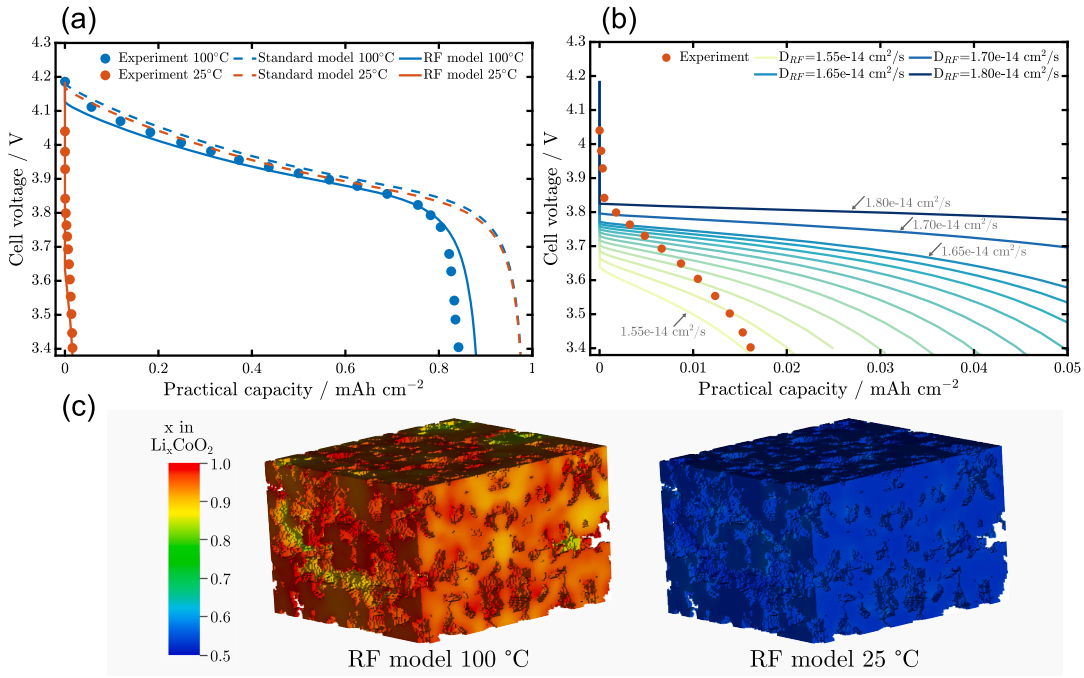

Fig. 6. (a) Comparison between experimental data (dotted lines) and simulation results for cell operation at 100 °C and 25 °C using two models: the standard interface model (dashed lines) and resistive film model (solid lines) with parameter sets HT1 and HT2, respectively. Resistive film parameters are: $l_{RF} = 100$ nm, $\sigma_{RF}^{CAM} = 1$ S/cm, $D_{RF}^{CAM} = 2{\cdot}10^{-13}$ cm^2/s at 100 °C and $D_{RF}^{CAM} = 1.55{\cdot}10^{-14}$ cm^2/s at 25 °C. The current is 0.1 mA/cm^2. (b) Influence of varying Li-ion mobility of a resistive film with a thickness of $l_{RF} = 100$ nm on cell performance at 25 °C. Between $D_{RF}^{CAM} = 1.55{\cdot}10^{-14}$ and $D_{RF}^{CAM} = 1.65{\cdot}10^{-14}$ cm^2/s, diffusivity is changed with increments of $0.01{\cdot}10^{-14}$ cm^2/s. (c) CAM phase lithiation state upon reaching the lower cut-off voltage, based on resistive film simulations at 100 and 25 °C.

standard interface model, we achieve good qualitative agreement with the experimental data for the 100 °C case. However, the simulated capacities are higher than in the experiments. At 25 °C, the difference between the simulations and the experimental data is much more pronounced. The experimental data shows an almost immediate voltage drop, while the simulation indicates capacities close to full utilization. Simulations with the standard interface model predict only minor differences between 100 and 25 °C.

However, using our resistive film model, we are able to reproduce the experimental data at 25 °C by adjusting the model parameters. The results of our sensitivity analysis suggest that a reduced Li-ion mobility of a secondary phase at the CAM/SE interface causes the observed capacity loss. An ohmic resistance is less significant at the low discharge rate of 0.1 mA/cm^2 (cf. Fig. 4(c)). By fitting D_{RF}^{CAM} at low and high temperatures, we can extract the diffusion coefficient as well as the activation energy assuming Arrhenius behavior (Eq. (11)).

$$D_{RF}^{CAM} = D_{RF,0}^{CAM} \cdot e^{-\frac{E_A}{RT}} \tag{11}$$

Our simulations indicate diffusivities of $2{\cdot}10^{-13}$ cm^2 /s at 100 °C and $1.55{\cdot}10^{-14}$ cm^2 /s at 25 °C. These results correspond to an activation energy of approximately E_A=0.04 eV.

Fig. 6 (b) shows the influence of the Li-ion mobility in the resistive film on the simulated discharge curve compared to the experimental data for the 25 °C case. A resistive film with low Li-ion mobility leads to a significant voltage drop at the onset of the discharge. Subsequently, the voltage decreases steadily until reaching the cut-off voltage at a very low capacity. Notably, the cell capacity and shape of the discharge curves fit qualitatively very well between experiments and simulations. Both the voltage offset at the beginning of the simulation and the capacity at the end of the discharge are strongly affected by the Li-ion mobility of the resistive film.

Fig. 6 (c) depicts the influence of the resistive film on the utilization of the CAM. For the 25 °C scenario, low Li-ion mobility within the resistive film results in pronounced blocking behavior of the SE/CAM interface and very low CAM utilization. Conversely, at 100 °C, enhanced Li-ion mobility in the interphase permits uniform lithiation.

Our results highlight the need for better interfacial stability of the CAM/SE interface by adjusting material selection and lowering sintering temperature. However, it is important to recognize the limitations of our model, which simplifies electrochemical transport across the interfacial layer under the assumption of a homogeneous resistive layer with uniform properties. Therefore, additional analysis is needed to confirm our simulation results. For example, interface-sensitive techniques such as high-resolution SIMS can offer valuable insights into secondary phase formation and its properties, especially when combined with three-dimensional tomography studies [53,54].

4.3. Analysis of the performance loss of low-temperature processed cells

To mitigate secondary phase formation during the manufacturing of oxide-based ASSB cells, new methods are being developed to reduce sintering temperature and dwell time. A promising approach is FAST/SPS, which utilizes high pressures to facilitate cathode densification at reduced temperatures and shorter dwell times. Ihrig et al. achieved a LCO/LLZO mixed cathode with a high density of 95% at sintering temperatures of 675–750 °C and dwell times of 10 min [29]. Subsequent SEM and TEM analyses revealed no secondary phase formation at the SE/CAM interface after the manufacturing process [30]. However, the ASSBs showed rapid capacity fade during cycling at 80 °C and 0.05 mA/cm^2. Detailed analysis of the SE/CAM interface indicated that electrochemical degradation of the interface and formation of resistive interphases impede charge transport [30,31]. A key role was attributed to Al in the SE phase, which, upon cycling, diffuses into the CAM phase [31]. In LLZO:Al, Al stabilizes the highly conductive cubic phase. Consequently, the movement of Al into the CAM can result in the formation of tetragonal or amorphous LLZO with reduced ionic conductivity. Additionally, it was proposed that Al obstructs Li-ion pathways in LCO upon diffusion [31].

In this section, we use microstructure-resolved simulations focusing on the degradation observed during cell operation to gain a better understanding of the underlying mechanisms.

4.3.1. Experimental results

Capacity fade Figure S3 shows the capacity fade of ASSBs with LCO/LLZO composite cathodes from Ref. [30] during the first ten cycles. The measured capacities are normalized to the theoretical capacity of the composite cathode as determined from the FIB-SEM reconstruction of sample LT (cf. Section 3.1). During the first discharge, the ASSB achieves a normalized capacity of about 75%. Approximately 25% of the CAM are not utilized. The capacity gradually decreases in subsequent cycles. The capacity fade is more prominent in the first few cycles. After ten cycles, the cell reaches a normalized capacity of around 40%. Similar capacity fade during electrochemical cycling has been observed by other research groups [24,32,55]. The significant performance loss of oxide-based ASSB cells is generally attributed to degradation at the CAM/SE interface resulting from mechanical, electrochemical, and chemical degradation [22,31,32].

SIMS analysis To investigate electrochemical degradation at different stages (uncycled and cycled), SIMS analysis was performed to map the elemental distribution in the composite cathode microstructure. Fig. 7 (a) and (b) display the experimental results for a pristine and cycled (10 cycles) sample. The yellow, red, and blue colors represent Al, Co, and La, respectively. The SIMS line profiles illustrate the elemental distribution across the LCO/LLZO:Al,Ta interface, with three representative profiles displayed for each sample. The position of the line graphs is indicated in the SIMS images by the white arrows.

In an ideal scenario with no interdiffusion, one would expect the Co signal to be confined to the LCO phase and the La and Al signals to be exclusively present in the LLZO:Al,Ta phase. This would result in a distinct correlation between the La and Al signals. However, the SIMS results for the pristine sample (Fig. 7 (a)) indicate that diffusion processes occur across the LCO/LLZO:Al,Ta interface during processing. Specifically, Al, initially in the LLZO:Al,Ta phase, redistributes and accumulates at the LCO/LLZO:Al,Ta interface. Line scans further reveal the formation of a diffusion zone with Al being detected well inside the LCO particles (≈ 500 nm from the CAM/SE interface, indicated by the black arrows). In addition to Al migration, there is evidence of minor Co and La interdiffusion at the LCO/LLZO:Al,Ta interface.

After cycling (Fig. 7 (b)), the Al signal correlates with the Co signal. This indicates that during cycling, Al diffuses into the LCO and forms a thermodynamically favorable interphase. Theoretical calculations suggest that the formation of Al-LCO is preferential at low lithiation states of LCO [31]. A redistribution of Al from LLZO into LCO during electrochemical cycling was also observed by Park et al. [23]. Interestingly, some LCO particles do not exhibit any Al signal, suggesting that they are electrochemically inactive [31]. To quantify this effect, we use image processing techniques to analyze the LCO fraction without an Al signal in three Regions of Interest (ROIs) from the SIMS measurements after cycling. We convert the original image to a binary format and calculate the fraction of LCO particles that show an overlap between Co and Al signals. The procedure is shown in more detail in Figure S4. On average, 84% of the LCO in the 2D image exhibit an Al signal after cycling, indicating that approximately 16% of the LCO is electrochemically inactive. It is important to note that estimating volume fractions from 2D images introduces some inherent error. However, we believe that the results obtained from the image analysis provide a reasonable estimate of the fraction of inactive CAM.

4.3.2. DFT calculations

Ihrig et al. proposed that Al-ions migrate from LLZO:Al,Ta to Li sites in LCO, thereby inhibiting Li-ion transport [31]. To evaluate the impact of Al on the chemical Li-ion diffusion coefficient in LCO, we perform density functional theory (DFT) simulations of both pristine and Al-contaminated LCO. LCO is modeled by a 2x2x1 supercell containing 12 Li atoms, 12 Co atoms, and 24 O atoms ($Li_{12}Co_{12}O_{24}$). We assume that a single Al atom occupies one Li position and consider the

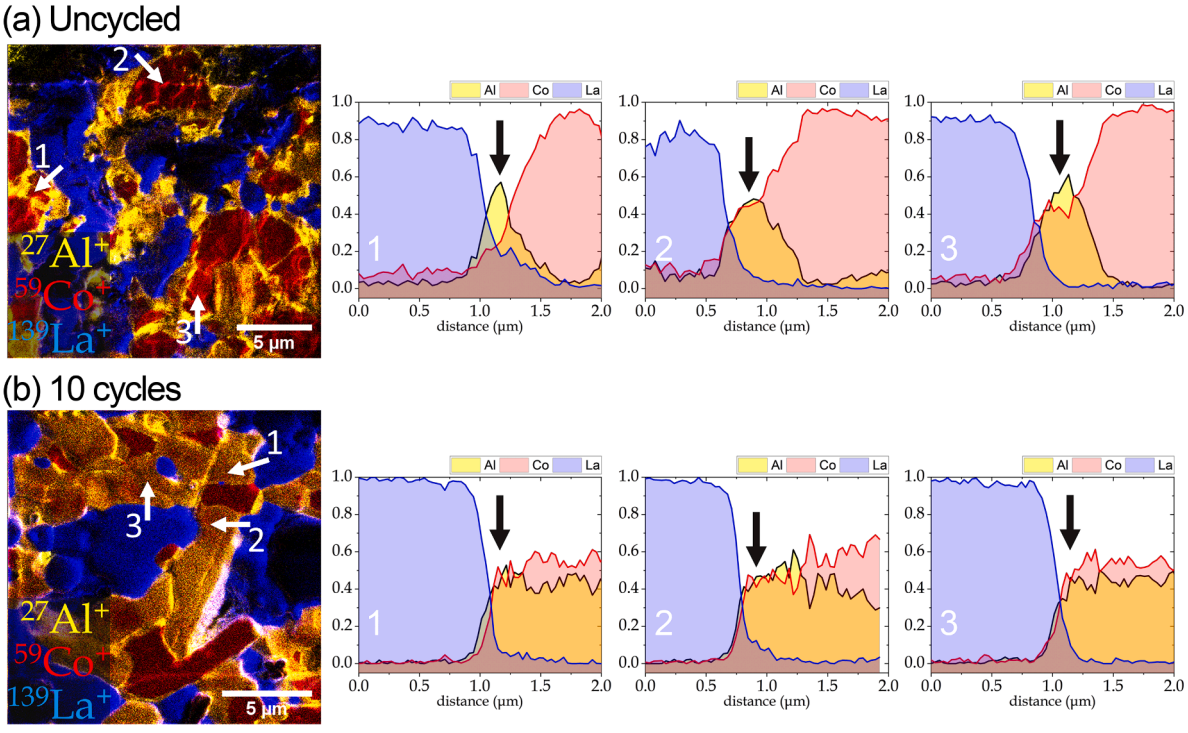

Fig. 7. (a) Elemental mapping for sample LT after manufacturing (uncycled) performed via SIMS. (b) Elemental mapping for sample LT after 10 cycles (cycled). Co signal is shown in red, La signal in blue, and Al signal in yellow. For each sample, three line profiles across the LLZO/LCO interface are shown, which are indicated by the white arrows in the elemental map. The count for each elemental signal is shown in relation to the total count of Co, La and Al for every pixel. Black arrows indicate the position of the interface LLZO/LCO.

additional removal of two Li atoms to achieve charge balance ($Li_9Al_1Co_{12}O_{24}$). The mass fraction of Al in the resulting Al-LCO phase is 2.3 wt.%. The removal of Li atoms in comparison to the pristine LCO phase not only reduces the maximum Li-ion concentration but also blocks Li-ion transport pathways. In the case of pristine LCO, our atomistic simulations yield a diffusion coefficient of $7.98{\cdot}10^{-12}$ cm^2 /s. This value is consistent with the concentration-dependent diffusion coefficient used in our structure-resolved simulations [51]. However, for the Al-LCO phase, the diffusion coefficient significantly decreases by approximately two orders of magnitude to $4.46{\cdot}10^{-14}$ cm^2/s. This suggests that Al diffusion can impede Li-ion transport in LCO, potentially acting as a limiting factor for cell performance. Further details regarding the DFT simulations are provided in the SI.

4.3.3. Structure-resolved simulations

The FIB-SEM reconstruction of sample LT, manufactured via FAST/SPS, shows a high sinter density, a balanced ratio of CAM to SE, and a low fraction of isolated CAM particles (cf. Table 1). Consequently, substantial kinetic limitations at low current densities are not anticipated. Our electrochemical simulations suggest that the normalized capacity is above 90% at a current density of 0.05 mA /cm^2 (cf. Figure S5: 0% Al-LCO).

In contrast, the measured capacity after the initial cycle is significantly lower, approximately 75%. This discrepancy is likely due to mechanical and electrochemical degradation during the first cycle. Additionally, despite the low sintering temperature and detailed analysis using TEM on the same materials reported in Ref. [30], we cannot exclude the formation of secondary phases at the LCO/LLZO interface during manufacturing. In fact, SIMS analysis shows interdiffusion for the pristine sample. Multiple degradation mechanisms are likely occurring in parallel, leading to the observed reduction in capacity.

Particle deactivation CAM particles are electrochemically inactive when they lose connection to either the ionic or electronic conduction networks. Our SIMS analysis indicates that approximately 16% of the LCO in the composite cathode is electrochemically inactiv (cf. Section 4.3.1). In contrast to most LCO particles, the inactive particles do not display any Al signal. Considering that Al-ion diffusion into LCO appears to be thermodynamically favorable, it is likely that these particles are already inactive after processing or become inactive during the first cycle. Interestingly, our FIB-SEM reconstruction shows below 1% of unconnected CAM particles. In contrast to the estimation of unconnected particles from the SIMS measurements, where we rely on the compositional information at the particle scale, the direct determination of cracks in FIB-SEM depends significantly on the available resolution and contrast. Some cracks or particle delamination might be below the typical resolution limit of FIB-SEM. Moreover, the volume of the FIB-SEM data only represents a limited section of the cathode due to the limited analysis area.

Electrochemical degradation According to our SIMS analysis, electrochemical cycling results in the gradual diffusion of Al-ions from the LLZO into the LCO phase, influencing both the CAM and SE properties. As proposed by Ihrig et al., Al-ions might migrate and occupy Li sites in the delithiated state of LCO [31]. This reduces the capacity of the CAM and the chemical diffusion coefficient (cf. Section 4.3.2). Furthermore, the diffusion of Al-ions can potentially destabilize the cubic phase of the LLZO electrolyte, thereby reducing its ionic conductivity. While Section 4.2 focuses on thin resistive layers (nanometer scale), the processes discussed in this section are on the micrometer scale.

Reduced number of Li sites and decreased Li-ion mobility To simulate the diffusion of Al-ions into the LCO particles, we create multiple simulation geometries with varying thickness of an Al-LCO layer extending from the CAM/SE interface into the LCO particles. The first step involves identifying the LCO/LLZO interface in the original cathode structure using an Euclidean distance transform. Once the interface is determined, we incrementally increase the thickness of the Al-LCO layer in multiples of the voxel size of 240 nm.

We generate six distinct geometries featuring Al-LCO thickness of 0 nm, 480 nm, 720 nm, 960 nm, and 1200 nm, as well as a case where all LCO is assumed to be contaminated with Al. Regarding our simulation geometry, these scenarios correspond to Al-LCO fractions of 0%, 32%, 58%, 67%, 80%, and 100% of the original LCO phase, respectively. Based on the results of our DFT simulations, we assume reduced Li-ion diffusivity ($D_{Li} = 4.46{\cdot}10^{-14}$ cm^2/s) in Al-LCO compared to pristine LCO, along with a reduced maximum Li-ion concentration (75% of its original value).

Fig. 8 (a) shows the measured capacity loss of an ASSB with LCO/LLZO cathode over ten cycles [30]. Our simulation results and the SIMS data allow us to attribute the observed performance to different degradation mechanisms. First, capacity is lost due to inactive CAM (blue bars). We assume 16% inactive CAM, determined from SIMS analysis. Second, active LCO particles are not fully utilized due to kinetic limitations (yellow bars). Our simulations with pristine LCO (0% Al-LCO) predict a reduction in normalized capacity of 8% (cf. Figure S5). These first two factors account for the performance loss in the pristine composite cathode before cycling. Any additional capacity loss beyond this baseline is attributed to chemical, electrochemical, and mechanical degradation, causing an increasing capacity loss upon cycling.

We compare the measured capacity after 10 cycles to the simulations assuming 100% Al-LCO. Since the FIB-SEM reconstruction shows a negligible fraction of inactive CAM particles, we subtract the additional 16% inactive CAM after the simulation. Interestingly, the simulations using the DFT data as input ($4.46{\cdot}10^{-14}$ cm^2/s) significantly overestimate the capacity loss after 10 cycles. The simulation predicts a 25% loss due to the reduced number of Li sites from Al diffusion and an additional 46% loss from the decreased Li mobility relative to pristine LCO. The resulting total capacity loss (71%) is significantly higher than the 36% loss observed experimentally. This discrepancy could be attributed to the assumptions made regarding a homogeneous blocking layer, which, in reality, might be much more heterogeneous. In fact, the LLZO (0.2 wt.% Al) in the composite cathode does not contain sufficient Al to provide a homogeneous Al-LCO phase for the whole CAM with the assumptions made in our DFT calculations (2.3 wt.% Al). While Al could potentially diffuse from the separator, the mobility and rate of Al-ion diffusion remain uncertain. Given the greater distance to the CAM, these diffusion processes might operate on an extended timescale, potentially surpassing the 10 cycles measured experimentally. Additionally, Al might exhibit some movement to the Co sites in LCO in the lithiated state, as proposed by Ihrig et al. [31].

Therefore, we extract an estimate of D_{Li} by fitting the capacity after 10 cycles assuming 100% Al-LCO. The fit yields an effective diffusion coefficient of around $6{\cdot}10^{-13}$ cm^2/s. Our simulation results suggest that the measured capacity loss can largely be attributed to reduced available Li sites in LCO. Additionally, particle delamination resulting from mechanical degradation, leading to a decreased CAM/SE interface area, could further exacerbate kinetic limitations induced by the diminished Li-ion mobility in the active material [55].

To provide insights into the growth dynamics of the Al-LCO layer during cycling, we conduct simulations on different geometries with varying Al-LCO phase layer thickness. In Fig. 8 (b), the simulated capacities are aligned with D_{Li} from DFT and the fit to the experimental data. The simulated values include a correction for the 16% performance loss arising from inactive particles. Increasing thickness of the Al-LCO layer directly correlates with a reduction in discharge capacity (cf. Figure S5). By correlating the simulated capacities associated with different Al-LCO layer thickness and the measured capacity in different cycles, we find that the majority of Al-LCO formation likely occurs during the initial cycles. Specifically, more than 50% of the LCO is contaminated with aluminum after just three cycles. The growth rate of this Al-LCO layer is predicted to slow down in subsequent cycles, leading to a more gradual decline in capacity. This corresponds to an expected

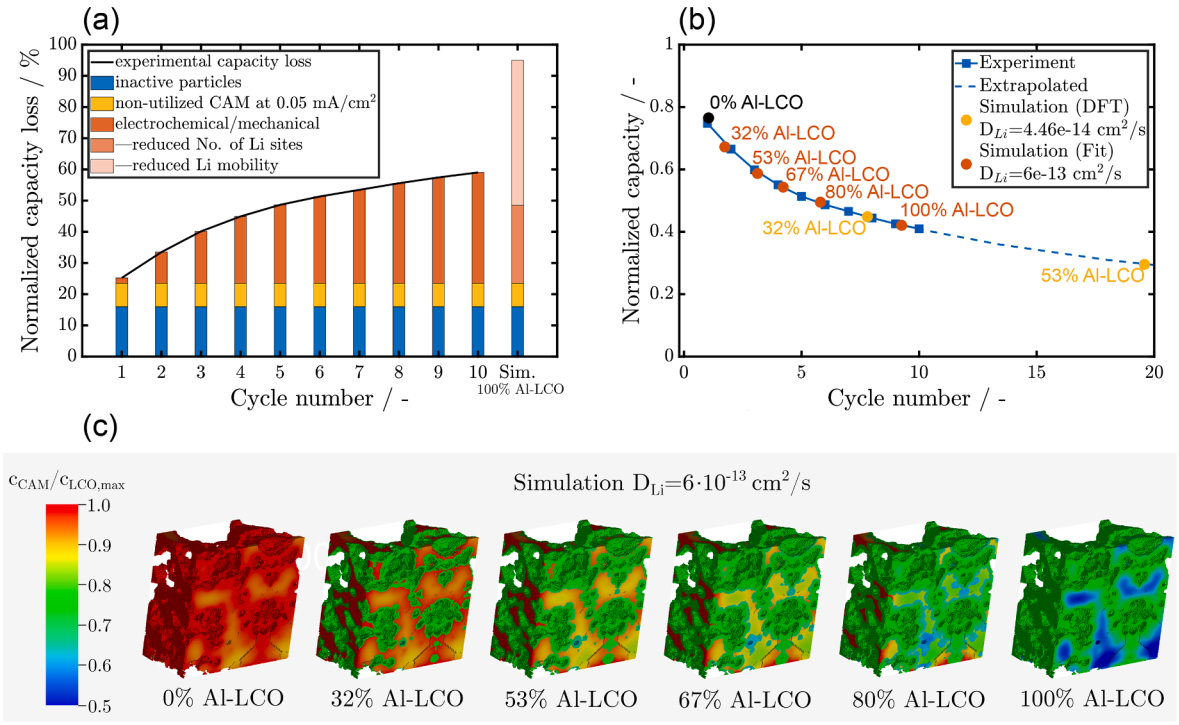

Fig. 8. Analysis of capacity loss due to Al-LCO phase propagation. (a) Comparison of experimental capacity loss over ten cycles with the simulation assuming 100% Al-LCO phase. Values are corrected for a 16% capacity loss due to inactive particles. (b) Aligned simulated and experimental capacities over cycling. Six geometries are examined, each with different Al-LCO layer thickness, corresponding to varying Al-LCO phase fractions. Simulated capacities are adjusted for a 16% loss due to inactive particles. (c) Li-ion concentration in the CAM after discharge for increasing Al-LCO layer thickness and $D_{Li} = 6{\cdot}10^{-13}$ cm^2/s. The separator is on the left and the current collector on the right of the depicted structures.

diffusion controlled growth of the Al-LCO interphase.

Fig. 8 (c) shows the Li-ion concentration in the CAM phase after discharge with increasing Al-LCO layer thickness. As the Al-LCO layer grows, the fraction of the CAM with reduced Li-ion capacity increases. Additionally, the lower Li-ion mobility in the Al-LCO layer reduces CAM utilization. Even a relatively thin Al-LCO layer is a significant transport barrier at the interface. These results are consistent with the experimental data suggesting that capacity fade is more prominent during the initial cycles. This effect is even enhanced for the low Li-ion mobility predicted by DFT calculations (cf. Figure S5).

Reduction of ionic conductivity Additionally, the loss of Al in the LLZO can cause the formation of tetragonal or amorphous LLZO with reduced ionic conductivity [23,31]. However, our electrochemical simulations indicate that this phase transition has a negligible impact on performance under the conditions studied. When we decrease the SE conductivity in the composite cathode by two orders of magnitude - which simulates the phase change from cubic to tetragonal LLZO [56] - the capacity at the current density of 0.05 mA/cm^2 only drops by approximately 1%. It is important to note that the impact of reduced electrolyte conductivity on cell performance becomes significantly more pronounced at elevated current densities, where fast charge transport kinetics are essential to achieve high capacities. The corresponding discharge curves are shown in Figure S6.

From our simulation results, we conclude that:

- The primary cause of performance loss during cycling appears to be electrochemical degradation, specifically the formation of an Al-LCO phase with reduced Li-ion mobility. Mechanical degradation seems to play a less significant role for the material system and under the operation conditions studied [30].
- The formation of the Al-LCO phase has two limiting effects: it lowers the overall concentration of Li sites in the active material. Additionally, it reduces Li-ion mobility at the CAM/SE interface.
- The rate of secondary phase formation appears to be more rapid in the initial cycles and slows down in subsequent cycles.
- At low current density, reduced electrolyte conductivity in the composite cathode, provoked by a phase transition from cubic to tetragonal LLZO, has minimal impact on overall cell capacity.

5. Conclusion

Secondary phases forming at the CAM/SE interface during manufacturing and cell cycling can significantly limit the performance of all-solid-state batteries and pose a significant challenge for cell development. To better understand the involved processes and limitations, we use structure-resolved simulations based on FIB-SEM reconstructions of LCO/LLZO cathodes. We introduce a new resistive film model to consider the influence of thin resistive films at the cathode/electrolyte interface. We can align simulation and experimental results at the cell level by utilizing effective parameters to describe secondary phases at the interface. This enables us to identify the key processes that limit cell performance. We investigate two main causes of degradation in all-solid-state batteries: thermally induced degradation of high-temperature processed electrodes and degradation during electrochemical cycling of low-temperature processed cells.

A key challenge of manufacturing LLZO-based composite cathodes is the high sintering temperatures necessary for good interfacial contact and densification. Despite high CAM utilization at 100 °C, very low measured capacities at room temperature suggest the presence of an additional charge transfer resistance with high activation energy after high-temperature sintering [22]. Our simulations indicate that a thin resistive film with reduced Li-ion mobility forms due to cation diffusion during sintering. The Li-ion mobility in the resistive film decreases at lower temperatures, blocking Li-ion transport at the CAM/SE interface. The slow charge transfer across the resistive film results in an isolation of CAM and a nearly instant drop in capacity upon discharge. In our study,

we estimate a low Li-ion diffusion coefficient in the resistive film of $1.55 \cdot 10^{-14}$ cm^2/s at 25 °C. Based on our simulations, for successful operation at practical current densities, it should not be significantly below $1 \cdot 10^{-12}$ cm^2/s.

During the electrochemical cycling of low-temperature processed cells, the LCO/LLZO cathode can experience mechanical and electrochemical degradation, resulting in a gradual loss of capacity. In our study, we use SIMS measurements to show that electrochemical cycling leads to the thermodynamically favorable diffusion of Al-ions from LLZO into the LCO phase. Al can block Li-ion transport pathways by occupying Li sites in the active material. DFT calculations show a significant reduction in Li-ion mobility for the resulting Al-LCO phase compared to pristine LCO. This study investigates the influence of a propagating Al-LCO layer with reduced Li-ion mobility and structural changes in the LLZO electrolyte, leading to reduced ionic conductivity, on cell performance through structure-resolved simulations. Our results indicate that mainly two mechanisms lead to the electrochemical performance loss during cycling. First, Al occupying Li sites reduces maximum Li-ion concentration in LCO and, thus, capacity. Second, an Al-LCO phase with reduced Li-ion mobility slows down charge transport and reduces the utilization of larger LCO particles. In contrast, at low current density, the possible transformation of cubic LLZO into its tetragonal or amorphous phase with reduced ionic conductivity due to Al loss or mechanical stresses has only a minor effect on cell performance. Our results indicate that interphase formation is more pronounced during the initial cycles and slows down with subsequent cycles. It is important to note that kinetic limitations at higher current densities will be more pronounced.

6. Outlook

For many commercial applications, operation at room temperature is crucial. Therefore, further research should focus on enhancing interface stability during sintering by improving material compatibility and reducing sintering temperature. To avoid interfacial degradation, stable interlayers could be used that show at least the electrochemical properties as determined in this study (At practical current densities: $R_{RF} \approx 1$ kΩ cm^2 and $D_{RF} \approx 1 \cdot 10^{-12}$ cm^2/s at a film thickness of 100 nm). Recent studies using sintering techniques such as FAST/SPS at high pressure and reduced sintering temperature have shown promising results [29–31]. Although sintering additives can lower sintering temperatures [57,58], they also reduce the theoretical energy density. An alternative approach is to explore concepts that avoid co-sintering entirely, for example, infiltrating an LLZO scaffold with LCO at a comparatively low synthesis temperature [27].

When applied to samples at various stages of degradation, our combined experimental and simulation approach can be used in future studies to determine the growth kinetics of resistive degradation layers during cycling. However, the investigation of resistive degradation films requires advanced characterization techniques for an experimental analysis of their composition and properties. This is crucial not only for enhancing the understanding of degradation processes but also for validating the results of computational studies.

The significant impact of electrochemical degradation highlights the need for effective coatings. Coating layers can improve interfacial stability at the CAM/SE interface, thereby preventing electrochemical degradation and improving rate capability and cycle life. An ideal coating layer must meet several requirements. Generally, coatings are employed to increase the electrochemical stability window. Their primary function is to act as a buffer layer, blocking electrons to prevent reactions between the SE and CAM while being ionically conductive to facilitate efficient ion transfer to the CAM. [40,59] Therefore, coatings should essentially function as stable SEs. Moreover, the coating layer must inhibit interdiffusion and the formation of interphases during high-temperature processing and electrochemical cycling, implying that the material should exhibit low mobility for all ions except lithium. [59] Promising coating materials for ASSBs include oxides such as Li_3BO_3 [16,60,61] and Li_3NbO_3 [62]. The electrochemical properties of these materials are influenced by their crystallinity, defects, and underlying microstructure. [62] Our resistive film model can be readily applied to simulate the influence of coating layers and aid in determining minimum values for critical electrochemical transport parameters, which are essential for theoretical and experimental materials screening. For typical ionic conductivities (up to 10^{-5} S/cm at room temperature) [63] and thin coating layers, the resultant ohmic resistance and its impact on electrochemical cell performance is minor (cf. Ohmic contributions in Section 4.1.1). However, it is important to note that incorporating a coating layer introduces two additional interfaces: one between the coating material and the SE, and the other between the coating material and the CAM. Charge transfer resistances at these interfaces must be minimized to ensure efficient charge transfer. Additionally, the coating must possess favorable mechanical properties to maintain intimate contact with both the CAM and SE, even during volume changes due to lithiation/delithiation. [59]

Supporting Information

Additional references cited within the Supporting Information [64].

CRediT authorship contribution statement

Moritz Clausnitzer: Writing – review & editing, Visualization, Validation, Software, Methodology, Investigation, Formal analysis, Conceptualization. **Martin Ihrig:** Writing – review & editing, Methodology, Investigation, Formal analysis, Conceptualization. **Luca Cressa:** Writing – review & editing, Visualization, Methodology, Investigation, Formal analysis, Conceptualization. **Simon Hein:** Software. **Martin Finsterbusch:** Conceptualization, Writing – review & editing. **Santhana Eswara:** Writing – review & editing, Supervision, Funding acquisition, Conceptualization. **Liang-Yin Kuo:** Writing – review & editing, Software, Methodology, Investigation, Formal analysis. **Timo Danner:** Writing – review & editing, Supervision, Methodology, Funding acquisition, Conceptualization. **Payam Kaghazchi:** Software, Supervision. **Dina Fattakhova-Rohlfing:** Funding acquisition. **Olivier Guillon:** Writing – review & editing, Supervision, Funding acquisition. **Arnulf Latz:** Writing – review & editing, Supervision, Funding acquisition.

Declaration of competing interest

There is no conflict of interest to declare. The authors declare that they have no known competing financial interests or personal relationships that could have appeared to influence the work reported in this paper.

Data availability

Data will be made available on request.

Acknowledgements

The authors acknowledge support with computational resources provided by the state of Baden-Wurttemberg through bwHPC and the German Research Foundation (DFG) through grant no INST 40/575-1 FUGG (JUSTUS 2 cluster). L.-Y.K. and P.K. gratefully acknowledge the computing time granted through JARA-HPC on the supercomputer JURECA at Forschungszentrum Jülich. We are thankful for the funding received from the German Federal Ministry of Education and Research (BMBF) as part of the FestBatt2 project (FKZ: 03XP0435A). We gratefully acknowledge the financial support by the German Federal Ministry

for Economic Affairs and Climate Action (BMWK) within the scope of the OptiKeraLyt project (FKZ: 03ETE016C). This work was financially supported by the US Department of Energy (DOE) and the German Federal Ministry of Education and Research (BMBF) as part of the CatSE^2 project (FKZ: 03XP0510D). This work was partly funded by the Luxembourg National Research Fund (FNR) through the grant INTER/MERA/20/13992061 (INTERBATT). We gratefully acknowledge the financial support by the project Adambatt (FKZ: 13XP0305A). M.I. thanks the Alexander-von-Humboldt Foundation and the Taiwanese National Science and Technology Council for funding (grant no.: 112-2927-I-011-505).

Supplementary material

Supplementary material associated with this article can be found, in the online version, at 10.1016/j.ensm.2024.103262.

References

[1] J.G. Kim, B. Son, S. Mukherjee, N. Schuppert, A. Bates, O. Kwon, M.J. Choi, H. Y. Chung, S. Park, A review of lithium and non-lithium based solid state batteries, J. Power Sources 282 (2015) 299–322.
[2] J. Janek, W.G. Zeier, A solid future for battery development, Nat. Energy 1 (9) (2016) 1–4.
[3] P. Albertus, V. Anandan, C. Ban, N. Balsara, I. Belharouak, J. Buettner-Garrett, Z. Chen, C. Daniel, M. Doeff, N.J. Dudney, et al., Challenges for and pathways toward Li-metal-based all-solid-state batteries, ACS Energy Lett. 6 (4) (2021) 1399–1404.
[4] C. Heubner, S. Maletti, H. Auer, J. Hüttl, K. Voigt, O. Lohrberg, K. Nikolowski, M. Partsch, A. Michaelis, From lithium-metal toward anode-free solid-state batteries: current developments, issues, and challenges, Adv. Funct. Mater. 31 (51) (2021) 2106608.
[5] S. Lou, F. Zhang, C. Fu, M. Chen, Y. Ma, G. Yin, J. Wang, Interface issues and challenges in all-solid-state batteries: lithium, sodium, and beyond, Adv. Mater. 33 (6) (2021) 2000721.
[6] C. Chen, M. Jiang, T. Zhou, L. Raijmakers, E. Vezhlev, B. Wu, T.U. Schülli, D. L. Danilov, Y. Wei, R.-A. Eichel, et al., Interface aspects in all-solid-state Li-based batteries reviewed, Adv. Energy Mater. 11 (13) (2021) 2003939.
[7] X. Miao, S. Guan, C. Ma, L. Li, C.-W. Nan, Role of interfaces in solid-state batteries, Adv. Mater. (2022) 2206402.
[8] Q. Liu, Z. Geng, C. Han, Y. Fu, S. Li, Y.-b. He, F. Kang, B. Li, Challenges and perspectives of garnet solid electrolytes for all solid-state lithium batteries, J. Power Sources 389 (2018) 120–134.
[9] K.J. Kim, M. Balaish, M. Wadaguchi, L. Kong, J.L. Rupp, Solid-state li-metal batteries: challenges and horizons of oxide and sulfide solid electrolytes and their interfaces, Adv. Energy Mater. 11 (1) (2021) 2002689.
[10] C. Wang, K. Fu, S.P. Kammampata, D.W. McOwen, A.J. Samson, L. Zhang, G. T. Hitz, A.M. Nolan, E.D. Wachsman, Y. Mo, et al., Garnet-type solid-state electrolytes: materials, interfaces, and batteries, Chem. Rev. 120 (10) (2020) 4257–4300.
[11] C.A. Geiger, E. Alekseev, B. Lazic, M. Fisch, T. Armbruster, R. Langner, M. Fechtelkord, N. Kim, T. Pettke, W. Weppner, Crystal chemistry and stability of $Li_7La_3Zr_2O_{12}$ garnet: a fast lithium-ion conductor, Inorg. Chem. 50 (3) (2011) 1089–1097.
[12] E. Rangasamy, J. Wolfenstine, J. Sakamoto, The role of Al and Li concentration on the formation of cubic garnet solid electrolyte of nominal composition $Li_7La_3Zr_2O_{12}$, Solid State Ion. 206 (2012) 28–32.
[13] Y. Li, C.-A. Wang, H. Xie, J. Cheng, J.B. Goodenough, High lithium ion conduction in garnet-type $Li_6La_3ZrTaO_{12}$, Electrochem. Commun. 13 (12) (2011) 1289–1292.
[14] H. Buschmann, S. Berendts, B. Mogwitz, J. Janek, Lithium metal electrode kinetics and ionic conductivity of the solid lithium ion conductors $Li_7La_3Zr_2O_{12}$ and $Li_{7-x}La_3Zr_{2-x}Ta_xO_{12}$ with garnet-type structure, J. Power Sources 206 (2012) 236–244.
[15] A.C. Moy, G. Häuschen, D. Fattakhova-Rohlfing, J.B. Wolfenstine, M. Finsterbusch, J. Sakamoto, The effects of aluminum concentration on the microstructural and electrochemical properties of lithium lanthanum zirconium oxide, J. Mater. Chem. A 10 (41) (2022) 21955–21972.
[16] C. Roitzheim, Y.J. Sohn, L.-Y. Kuo, G. Haäuschen, M. Mann, D. Sebold, M. Finsterbusch, P. Kaghazchi, O. Guillon, D. Fattakhova-Rohlfing, All-solid-state Li batteries with NCM-garnet-based composite cathodes: the impact of NCM composition on material compatibility, ACS Appl. Energy Mater. 5 (6) (2022) 6913–6926.
[17] L. Miara, A. Windmüller, C.-L. Tsai, W.D. Richards, Q. Ma, S. Uhlenbruck, O. Guillon, G. Ceder, About the compatibility between high voltage spinel cathode materials and solid oxide electrolytes as a function of temperature, ACS Appl. Mater. Interfaces 8 (40) (2016) 26842–26850.
[18] L.J. Miara, W.D. Richards, Y.E. Wang, G. Ceder, First-principles studies on cation dopants and electrolyte|cathode interphases for lithium garnets, Chem. Mater. 27 (11) (2015) 4040–4047.
[19] N. Zhang, X. Long, Z. Wang, P. Yu, F. Han, J. Fu, G. Ren, Y. Wu, S. Zheng, W. Huang, et al., Mechanism study on the interfacial stability of a lithium garnet-type oxide electrolyte against cathode materials, ACS Appl. Energy Mater. 1 (11) (2018) 5968–5976.
[20] Y. Zhu, X. He, Y. Mo, First principles study on electrochemical and chemical stability of solid electrolyte–electrode interfaces in all-solid-state Li-ion batteries, J. Mater. Chem. A 4 (9) (2016) 3253–3266.
[21] G. Vardar, W.J. Bowman, Q. Lu, J. Wang, R.J. Chater, A. Aguadero, R. Seibert, J. Terry, A. Hunt, I. Waluyo, et al., Structure, chemistry, and charge transfer resistance of the interface between $Li_7La_3Zr_2O_{12}$ electrolyte and $LiCoO_2$ cathode, Chem. Mater. 30 (18) (2018) 6259–6276.
[22] M. Finsterbusch, T. Danner, C.-L. Tsai, S. Uhlenbruck, A. Latz, O. Guillon, High capacity garnet-based all-solid-state lithium batteries: fabrication and 3D-microstructure resolved modeling, ACS Appl. Mater. Interfaces 10 (26) (2018) 22329–22339.
[23] K. Park, B.-C. Yu, J.-W. Jung, Y. Li, W. Zhou, H. Gao, S. Son, J.B. Goodenough, Electrochemical nature of the cathode interface for a solid-state lithium-ion battery: interface between $LiCoO_2$ and garnet-$Li_7La_3Zr_2O_{12}$, Chem. Mater. 28 (21) (2016) 8051–8059.
[24] C.-L. Tsai, Q. Ma, C. Dellen, S. Lobe, F. Vondahlen, A. Windmüller, D. Grüner, H. Zheng, S. Uhlenbruck, M. Finsterbusch, et al., A garnet structure-based all-solid-state Li battery without interface modification: resolving incompatibility issues on positive electrodes, Sustain. Energy Fuels 3 (1) (2019) 280–291.
[25] X. Huang, C. Shen, K. Rui, J. Jin, M. Wu, X. Wu, Z. Wen, Influence of $La_2Zr_2O_7$ additive on densification and Li^+ conductivity for Ta-doped $Li_7La_3Zr_2O_{12}$ garnet, Jom 68 (2016) 2593–2600.
[26] L. Yang, X. Huang, C. Zou, X. Tao, L. Liu, K. Luo, P. Zeng, Q. Dai, Y. Li, L. Yi, et al., Rapid preparation and performances of garnet electrolyte with sintering aids for solid-state Li–S battery, Ceram. Int. 47 (13) (2021) 18196–18204.
[27] K.J. Kim, J.L. Rupp, All ceramic cathode composite design and manufacturing towards low interfacial resistance for garnet-based solid-state lithium batteries, Energy Environ. Sci. 13 (12) (2020) 4930–4945.
[28] M. Bitzer, T. Van Gestel, S. Uhlenbruck, et al., Sol-gel synthesis of thin solid $Li_7La_3Zr_2O_{12}$ electrolyte films for Li-ion batteries, Thin Solid Films 615 (2016) 128–134.
[29] M. Ihrig, M. Finsterbusch, C.-L. Tsai, A.M. Laptev, C.-H. Tu, M. Bram, Y.J. Sohn, R. Ye, S. Sevinc, S.-K. Lin, et al., Low temperature sintering of fully inorganic all-solid-state batteries–impact of interfaces on full cell performance, J. Power Sources 482 (2021) 228905.
[30] M. Ihrig, M. Finsterbusch, A.M. Laptev, C.-H. Tu, N.T.T. Tran, C.-A. Lin, L.-Y. Kuo, R. Ye, Y.J. Sohn, P. Kaghazchi, et al., Study of $LiCoO_2/Li_7La_3Zr_2O_{12}$: Ta interface degradation in all-solid-state lithium batteries, ACS Appl. Mater. Interfaces 14 (9) (2022) 11288–11299.
[31] M. Ihrig, L.-Y. Kuo, S. Lobe, A.M. Laptev, C.-A. Lin, C.-H. Tu, R. Ye, P. Kaghazchi, L. Cressa, S. Eswara, et al., Thermal recovery of the electrochemically degraded $LiCoO_2/Li_7La_3Zr_2O_{12}$: Al, Ta interface in an all-solid-state lithium battery, ACS Appl. Mater. Interfaces 15 (3) (2023) 4101–4112.
[32] A.-Y. Hou, C.-Y. Huang, C.-L. Tsai, C.-W. Huang, R. Schierholz, H.-Y. Lo, H. Tempel, H. Kungl, R.-A. Eichel, J.-K. Chang, et al., All-solid-state garnet-based lithium batteries at work-in operando TEM investigations of delithiation/lithiation process and capacity degradation mechanism, Adv. Sci. 10 (5) (2022) 2205012.
[33] R. Mücke, M. Finsterbusch, P. Kaghazchi, D. Fattakhova-Rohlfing, O. Guillon, Modelling electro-chemical induced stresses in all-solid-state batteries: anisotropy effects in cathodes and cell design optimisation, J. Power Sources 489 (2021) 229430.
[34] R. Koerver, W. Zhang, L. de Biasi, S. Schweidler, A.O. Kondrakov, S. Kolling, T. Brezesinski, P. Hartmann, W.G. Zeier, J. Janek, Chemo-mechanical expansion of lithium electrode materials–on the route to mechanically optimized all-solid-state batteries, Energy Environ. Sci. 11 (8) (2018) 2142–2158.
[35] F. Single, A. Latz, B. Horstmann, Identifying the mechanism of continued growth of the solid–electrolyte interphase, ChemSusChem 11 (12) (2018) 1950–1955.
[36] F. Single, B. Horstmann, A. Latz, Theory of impedance spectroscopy for lithium batteries, J. Phys. Chem. C 123 (45) (2019) 27327–27343.
[37] ITWM, Battery and electrochemistry simulation tool, (Available at https://www.itwm.fraunhofer.de/en/departments/sms/products-services/best-battery-electrochemistry-simulation-tool.html), Accessed: 07 November 2023.
[38] M. Clausnitzer, R. Mücke, F. Al-Jaljouli, S. Hein, M. Finsterbusch, T. Danner, D. Fattakhova-Rohlfing, O. Guillon, A. Latz, Optimizing the composite cathode microstructure in all-solid-state batteries by structure-resolved simulations, Batter. Supercaps 6 (11) (2023) e202300167.
[39] P. Minnmann, L. Quillman, S. Burkhardt, F.H. Richter, J. Janek, Quantifying the impact of charge transport bottlenecks in composite cathodes of all-solid-state batteries, J. Electrochem. Soc. 168 (4) (2021) 040537.
[40] P. Minnmann, F. Strauss, A. Bielefeld, R. Ruess, P. Adelhelm, S. Burkhardt, S. L. Dreyer, E. Trevisanello, H. Ehrenberg, T. Brezesinski, et al., Designing cathodes and cathode active materials for solid-state batteries, Adv. Energy Mater. 12 (35) (2022) 2201425.
[41] T. Shi, Q. Tu, Y. Tian, Y. Xiao, L.J. Miara, O. Kononova, G. Ceder, High active material loading in all-solid-state battery electrode via particle size optimization, Adv. Energy Mater. 10 (1) (2020) 1902881.
[42] L. Froboese, J.F. van der Sichel, T. Loellhoeffel, L. Helmers, A. Kwade, Effect of microstructure on the ionic conductivity of an all solid-state battery electrode, J. Electrochem. Soc. 166 (2) (2019) A318.
[43] A. Bielefeld, D.A. Weber, R. Rueß, V. Glavas, J. Janek, Influence of lithium ion kinetics, particle morphology and voids on the electrochemical performance of

composite cathodes for all-solid-state batteries, J. Electrochem. Soc. 169 (2) (2022) 020539.
[44] M. Rosen, M. Finsterbusch, O. Guillon, D. Fattakhova-Rohlfing, Free standing dual phase cathode tapes–scalable fabrication and microstructure optimization of garnet-based ceramic cathodes, J. Mater. Chem. A 10 (5) (2022) 2320–2326.
[45] A. Latz, J. Zausch, Thermodynamic consistent transport theory of Li-ion batteries, J. Power Sources 196 (6) (2011) 3296–3302.
[46] A. Latz, J. Zausch, Multiscale modeling of lithium ion batteries: thermal aspects, Beilstein J. Nanotechnol. 6 (1) (2015) 987–1007.
[47] S. Wang, H. Xu, W. Li, A. Dolocan, A. Manthiram, Interfacial chemistry in solid-state batteries: formation of interphase and its consequences, J. Am. Chem. Soc. 140 (1) (2018) 250–257.
[48] M. Landstorfer, S. Funken, T. Jacob, An advanced model framework for solid electrolyte intercalation batteries, Phys. Chem. Chem. Phys. 13 (28) (2011) 12817–12825.
[49] P. Ramadass, B. Haran, P.M. Gomadam, R. White, B.N. Popov, Development of first principles capacity fade model for Li-ion cells, J. Electrochem. Soc. 151 (2) (2004) A196.
[50] J. Molenda, A. Stokłosa, T. Bak, Modification in the electronic structure of cobalt bronze Li_xCoO_2 and the resulting electrochemical properties, Solid State Ion. 36 (1-2) (1989) 53–58.
[51] H. Xia, L. Lu, G. Ceder, Li diffusion in $LiCoO_2$ thin films prepared by pulsed laser deposition, J. Power Sources 159 (2) (2006) 1422–1427.
[52] Y. Ren, T. Danner, A. Moy, M. Finsterbusch, T. Hamann, J. Dippell, T. Fuchs, M. Müller, R. Hoft, A. Weber, et al., Oxide-based solid-state batteries: a perspective on composite cathode architecture, Adv. Energy Mater. 13 (1) (2023) 2201939.
[53] F. Walther, R. Koerver, T. Fuchs, S. Ohno, J. Sann, M. Rohnke, W.G. Zeier, J. Janek, Visualization of the interfacial decomposition of composite cathodes in argyrodite-based all-solid-state batteries using time-of-flight secondary-ion mass spectrometry, Chem. Mater. 31 (10) (2019) 3745–3755.
[54] L. Cressa, J. Fell, C. Pauly, Q.H. Hoang, F. Mücklich, H.-G. Herrmann, T. Wirtz, S. Eswara, A FIB-SEM based correlative methodology for X-ray nanotomography and secondary ion mass spectrometry: an application example in lithium batteries research, Microsc. Microanal. 28 (6) (2022) 1890–1895.
[55] R. Koerver, I. Aygün, T. Leichtweiß, C. Dietrich, W. Zhang, J.O. Binder, P. Hartmann, W.G. Zeier, J. Janek, Capacity fade in solid-state batteries: interphase formation and chemomechanical processes in nickel-rich layered oxide cathodes and lithium thiophosphate solid electrolytes, Chem. Mater. 29 (13) (2017) 5574–5582.
[56] T. Thompson, J. Wolfenstine, J.L. Allen, M. Johannes, A. Huq, I.N. David, J. Sakamoto, Tetragonal vs. cubic phase stability in Al–free Ta doped $Li_7La_3Zr_2O_{12}$ (LLZO), J. Mater. Chem. A 2 (33) (2014) 13431–13436.
[57] S. Ohta, J. Seki, Y. Yagi, Y. Kihira, T. Tani, T. Asaoka, Co-sinterable lithium garnet-type oxide electrolyte with cathode for all-solid-state lithium ion battery, J. Power Sources 265 (2014) 40–44.
[58] N. Rosero-Navarro, T. Yamashita, A. Miura, M. Higuchi, K. Tadanaga, Preparation of $Li_7La_3(Zr_{2-x}Nb_x)O_{12}$ (x= 0–1.5) and $Li_3BO_3/LiBO_2$ composites at low temperatures using a sol–gel process, Solid State Ion. 285 (2016) 6–12.
[59] S.P. Culver, R. Koerver, W.G. Zeier, J. Janek, On the functionality of coatings for cathode active materials in thiophosphate-based all-solid-state batteries, Adv. Energy Mater. 9 (24) (2019) 1900626.
[60] E.J. Cheng, Y. Kushida, T. Abe, K. Kanamura, Degradation mechanism of all-solid-state Li-metal batteries studied by electrochemical impedance spectroscopy, ACS Appl. Mater. Interfaces 14 (36) (2022) 40881–40889.
[61] E.J. Cheng, R. Oyama, T. Abe, K. Kanamura, High-voltage all-solid-state lithium metal batteries prepared by aerosol deposition, J. Eur. Ceram. Soc. 43 (5) (2023) 2033–2038.
[62] F. Walther, F. Strauss, X. Wu, B. Mogwitz, J. Hertle, J. Sann, M. Rohnke, T. Brezesinski, J. Janek, The working principle of a $Li_2CO_3/LiNbO_3$ coating on NCM for thiophosphate-based all-solid-state batteries, Chem. Mater. 33 (6) (2021) 2110–2125.
[63] A. Glass, K. Nassau, T. Negran, Ionic conductivity of quenched alkali niobate and tantalate glasses, J. Appl. Phys. 49 (9) (1978) 4808–4811.
[64] M. Weiss, R. Ruess, J. Kasnatscheew, Y. Levartovsky, N.R. Levy, P. Minnmann, L. Stolz, T. Waldmann, M. Wohlfahrt-Mehrens, D. Aurbach, et al., Fast charging of lithium-ion batteries: a review of materials aspects, Adv. Energy Mater. 11 (33) (2021) 2101126.